

Electronic Structure of Chromium Trihalides beyond Density Functional Theory

Swagata Acharya,^{1,*} Dimitar Pashov,² Brian Cunningham,³ Alexander N. Rudenko,¹
Malte Rösner,¹ Myrta Grüning,⁴ Mark van Schilfhaarde,^{2,5} and Mikhail I. Katsnelson¹

¹*Institute for Molecules and Materials, Radboud University, NL-6525 AJ Nijmegen, The Netherlands*
²*King's College London, Theory and Simulation of Condensed Matter, The Strand, WC2R 2LS London, UK*

³*Centre for Theoretical Atomic, Molecular and Optical Physics,
Queen's University Belfast, Belfast BT71NN, Northern Ireland, United Kingdom*

⁴*Atomistic Simulation Centre, Queen's University Belfast,
Belfast BT71NN, Northern Ireland, United Kingdom*

⁵*National Renewable Energy Laboratory, Golden, CO 80401, USA*

We explore the electronic band structure of free standing monolayers of chromium trihalides, CrX_3 , $X = \text{Cl}, \text{Br}, \text{I}$, within an advanced *ab-initio* theoretical approach based in the use of Green's function functionals. We compare the local density approximation with the quasi-particle self-consistent GW approximation (QSGW) and its self-consistent extension (QSGW \widehat{W}) by solving the particle-hole ladder Bethe-Salpeter equations to improve the effective interaction W . We show that at all levels of theory, the valence band consistently changes shape in the sequence $\text{Cl} \rightarrow \text{Br} \rightarrow \text{I}$, and the valence band maximum shifts from the M point to the Γ point. However, the details of the transition, the one-particle bandgap, and the eigenfunctions change considerably going up the ladder to higher levels of theory. The eigenfunctions become more directional, and at the M point there is a strong anisotropy in the effective mass. Also the dynamic and momentum dependent self energy shows that QSGW \widehat{W} adds to the localization of the systems in comparison to the QSGW thereby leading to a narrower band and reduced amount of halogens in the valence band manifold.

With the discovery of ferromagnetic order in CrI_3 , the family of chromium trihalides CrX_3 , $X = \text{Cl}, \text{Br}, \text{I}$, has emerged as a new class of magnetic 2D crystals. Ferromagnetism (FM) in a monolayer CrI_3 was first reported in 2017,^{1,2} which was followed by observation of FM in CrBr_3 ,^{3,4} CrCl_3 ⁵ and many other compounds.⁶⁻¹⁰ FM is intrinsic to these system, which distinguishes them from traditional 2D *sp*-electron magnets where magnetism is induced by proximity to a FM substrate. Long range-order is typically suppressed in two-dimensional magnets,¹¹ but it can be stabilized by magneto-crystalline anisotropy, which opens an energy gap in the magnon spectra and therefore protects the FM in two dimensions.^{12,13} Due to their layered structure and their weak inter-layer van-der-Waals interactions these systems are loosely coupled to their substrates, which provides greater flexibility in functionalizing them and controlling their properties, e.g. by varying the layer-number or by applying a gate voltage. This offers new possibilities to make spintronic devices with high accuracy and efficiency.^{2,14-22}

CrX_3 is a two-dimensional FM insulator with FM originating from the Cr-X-Cr superexchange interaction.^{13,23-25} Six Cr^{3+} ions form a honeycomb structure with D_{3d} point group symmetry and each Cr is surrounded by six X in an octahedral geometry (see Fig. 1). The edge-sharing geometry leads to first neighbor Cr atoms sharing a pair of ligands. This enables pathways for Cr-X-Cr super-exchange. In this crystal field geometry, the Cr *d* splits into a t_{2g} triplet and an e_g doublet. Cr^{3+} has a valence of three electrons, which fill the t_{2g} majority-spin band according to Hund's first rule, leaving all other *d* bands empty. The ionic model leads to the magnetic moment on each Cr^{3+} ion of $\sim 3\mu_B$ which

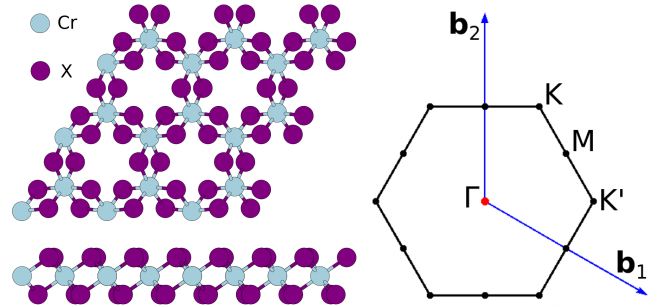


Figure 1. Left: Ball-and-stick model of the crystal structure of monolayer chromium trihalides CrX_3 ($X = \text{Cl}, \text{Br}, \text{I}$). Right: Brillouin zone of the corresponding hexagonal lattice with the high-symmetry points indicated. \mathbf{b}_1 and \mathbf{b}_2 denote reciprocal lattice vectors.

is confirmed by *ab-initio* calculations. All three CrX_3 compounds have FM order down to the monolayer with Curie temperatures $T_I = 45 \text{ K}$,¹ $T_{Br} = 34 \text{ K}$ ³ and $T_{Cl} = 17 \text{ K}$ ⁵ and the magnetization easy axis is normal to the plane for CrI_3 and CrBr_3 while it is in plane for CrCl_3 .

Recent Density Functional Theory (DFT) calculations²⁶⁻²⁸ confirm the qualitative understandings derived from the ionic model. However, at quantitative level details start to differ from the fully ionic picture; one important such factor is the degree of hybridization of the t_{2g} levels with the *p* bands of the ligands. This degree of hybridization depends on the ligand, its atomic weight and the number of core levels, which turns out to be a crucially important factor in determining the detailed electronic band structure. This is the main

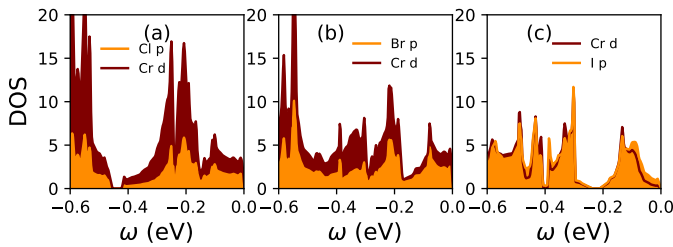


Figure 2. Partial Density of states within the LDA, projected onto the Cr- d and X- p states for (a) X=Cl, (b) Br and (c) I.

focus of the present paper which we carefully analyze on different levels of theory beyond conventional density functional theory. Our self-consistent GW (QSGW) and BSE (QSGW) implementations are independent of the starting point and, hence, allow us to study the roles of self-consistent charge densities and self-energies in determining the key features of the electronic structures at different levels of the theory.

Molecular Picture

Within the local-density approximation (LDA), we find the spin-polarized bandgaps of the three systems to be, 1.51 eV, 1.30 eV and 1.20 eV for X=(Cl, Br, I) respectively, in line with prior work.²⁶ The qualitative trend is easily understood in terms of the splitting between Cr d and X p atomic levels. In the simplest two-level tight-binding description, the conduction and valence levels are given by $(\varepsilon_d + \varepsilon_p)/2 \pm \sqrt{((\varepsilon_d - \varepsilon_p)/2)^2 + v^2}$, where ε_d and ε_p are respectively the Cr t_{2g} d and X p atomic levels and v the hybridization matrix element. This results in a gap $E_g = \varepsilon_d - \varepsilon_p + 2v^2/(\varepsilon_d - \varepsilon_p)$ to the lowest order in $v/(\varepsilon_d - \varepsilon_p)$. Among all three halides Iodine has the most core levels resulting in its p levels having the most nodes which thus sense the attractive nucleus most weakly. It has the shallowest ε_p of the three halogens, while Cl has the deepest. Thus, the qualitative trend in the bandgap is simply understood as following from the halide ε_p energies relative to the Cr ε_d . As a slight elaboration on this picture that includes magnetism, we can distinguish between the majority (t_{2g}^\uparrow) and minority (t_{2g}^\downarrow) Cr d levels. For the bandgap, the picture just sketched corresponds to the $(\varepsilon_d^\downarrow - \varepsilon_p)$ bond. A similar picture applies to the $\varepsilon_d^\uparrow - \varepsilon_p$ bond, but in this channel both bond and antibond are occupied, and moreover $\varepsilon_d^\uparrow - \varepsilon_p$ need not be large in comparison to v . Indeed the Cr t_{2g}^\uparrow and X p levels may overlap.

Energy band picture

The molecular picture qualitatively explains the trends in the bandgap and the admixture of X p in the highest valence states in the sequence Cl \rightarrow Br \rightarrow I. However, in the 2D crystal, the molecular levels broaden into bands which can alter the trends in both the bandgap and the merging

theory	bandgap (eV)			spectral weight		
	CrCl ₃	CrBr ₃	CrI ₃	CrCl ₃	CrBr ₃	CrI ₃
DFT	1.51	1.30	1.06	24%	31%	50%
QSGW	6.87	5.73	3.25	45%	69%	84%
QSGW \widehat{W}	5.55	4.65	2.9	27%	37%	71%

Table I. One particle electronic band gap at different levels of theory (with spin-orbit coupling). The gap increases from LDA to QSGW level. When ladder diagrams are added two-particle interactions via a BSE, $W \rightarrow \widehat{W}$ and screening is increased. This reduces the QSGW bandgap. Right columns show fraction of spectral weight that the Halogen contributes to the total DOS within an energy window of occupied states ($-0.6, 0$) eV, relative to the valence band maximum.

of X p with Cr t_{2g}^\uparrow in the valence bands. The corresponding orbital resolved density of states are shown in Fig. 2. The X p level becomes more shallow, and the highest lying valence band acquires increasing anion character as can be seen both in Table I and in Fig. 2. Spin-orbit coupling only slightly modifies the electronic structure for CrCl₃ and CrBr₃, while for CrI₃ the bandgap reduces by 150 meV to 1.06 eV in the LDA.

However, as is typical of the LDA, the bandgaps are underestimated, and for CrX₃ the underestimation is severe. Accordingly, we study the electronic structure at three different levels of theory: the LDA, the Quasiparticle Self-Consistent GW approximation (QSGW),^{29,30} and an extension of QSGW where the RPA approximation to the polarizability is extended by adding ladder diagrams (QSGW \widehat{W}).^{31,32} The electronic dispersions and corresponding DOS are shown in Figs. 3,4,5, for each level of theory and each material. In contrast to typical sp semiconductors, not only the bandgaps but also the valence band dispersions significantly change as the level of theory increases.

QSGW dramatically enhances the gaps relative to the LDA, as is standard in polar compounds.²⁹ Nevertheless, within the random phase approximation (RPA), it has long been known that W is universally too large,^{33,34} and this is reflected in an underestimate of the static dielectric constant ϵ_∞ . Empirically, ϵ_∞ seems to be underestimated in QSGW by a nearly universal factor of 0.8, for a wide range of insulators.^{35,36} Roughly speaking, at low energy W is universally too large by a factor $1/0.8$ ³⁷ and as a result, QSGW bandgaps are slightly overestimated.²⁹ This can be corrected by extending the RPA to introduce an electron-hole attraction in virtual excitations. These extra (ladder) diagrams are solved by a BSE, and they significantly improve on the optics, largely eliminating the discrepancy in ϵ_∞ .³¹ When ladders are also added to improve W in the GW cycle ($W \rightarrow \widehat{W}$), it significantly improves the one-particle gap as well, as will be discussed elsewhere.³² This scenario is played out in CrX₃ compounds: QSGW bandgaps are slightly larger than QSGW \widehat{W} bandgaps, as seen in Table I.

Remarkably, the structure of the valence band is very

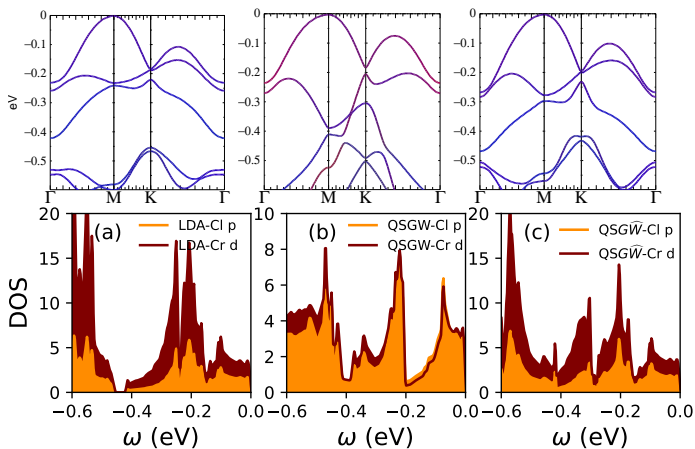


Figure 3. CrCl_3 : From left to right: LDA, QSGW and $\widehat{\text{QSGW}}$ valence band structures (with spin-orbit coupling) are shown respectively. The colors correspond to Cl- $p_x + p_y$ (red), Cl- p_z (green), Cr-d (blue). In the bottom panels are shown the density of states projected onto the Cr-d and Cl-p states at different levels of the theory.

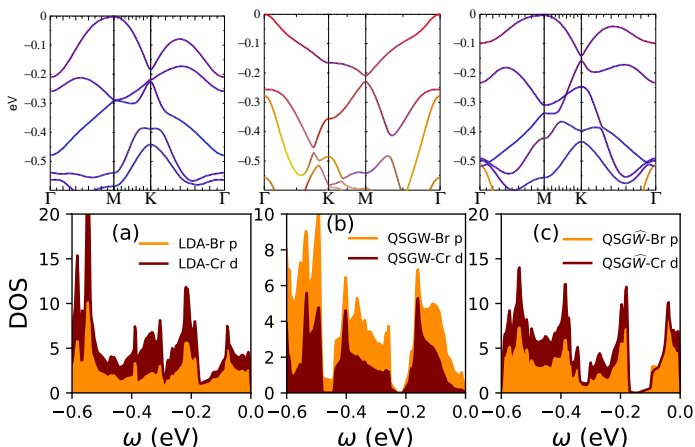


Figure 4. CrBr_3 : From left to right: LDA, QSGW and $\widehat{\text{QSGW}}$ valence band structures (with spin-orbit coupling) are shown respectively. The colors correspond to Br- $p_x + p_y$ (red), Br- p_z (green), Cr-d (blue). In the bottom panels are shown the density of states projected onto the Cr-d and Br-p states at different levels of the theory. Structure of the top most valence band is similar within LDA and $\widehat{\text{QSGW}}$, but is different in QSGW. the $\widehat{\text{QSGW}}$ top most valence band is much narrower in comparison to both QSGW and LDA and is split from the rest of the valence band manifold.

sensitive to the level of theory used, which applies to both, the band energies and wave functions. Just for CrCl_3 the valence band maximum is independent of the theory and is consistently pinned to the M point (Fig. 3). In the sequence Cl \rightarrow Br \rightarrow I, there is an overall tendency for the valence band maximum to shift from the M point to the Γ point. In the LDA this transition occurs af-

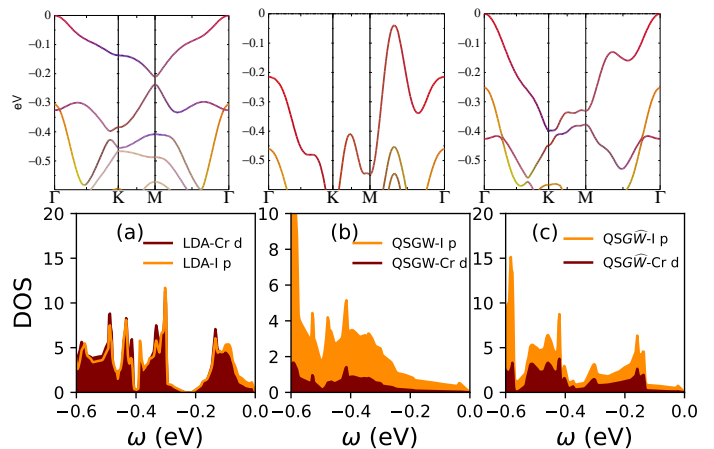


Figure 5. CrI_3 : From left to right: LDA, QSGW and $\widehat{\text{QSGW}}$ valence band structures (with spin-orbit coupling) are shown respectively. The colors correspond to I- $p_x + p_y$ (red), I- p_z (green), Cr-d (blue). In the bottom panels are shown the density of states projected onto the Cr-d and I-p states at different levels of the theory. Note that in the QSGW case, the valence band maximum is at a low-symmetry point not on the lines of the figure.

theory	CrCl_3		CrBr_3		CrI_3	
	m_x	m_y	m_x	m_y	m_x	m_y
DFT	1.9	3.6	2.0	5.2	1.2	1.2
QSGW	2.3	5.5	∞	-1.3	1.4	1.4
$\widehat{\text{QSGW}}$	2.1	4.2	3.2	∞	0.57	0.57

Table II. Effective masses m^*/m_0 at the M point (as shown in Fig. 1) for CrCl_3 and CrBr_3 , and at the Γ point for CrI_3 , for three levels of approximation. These k points correspond to the valence band maximum except for CrBr_3 in the QSGW approximation (see Fig. 5). m_x and m_y correspond to orientations perpendicular and parallel to the Γ -M line, respectively. ∞ is a shorthand for an effective mass larger than $10m_0$.

ter Br and I, while in QSGW the valence band at Γ is above M already for Br. $\widehat{\text{QSGW}}$ shows the same tendency as QSGW, but the change is less pronounced and the transition takes place between Br and I. This is a reflection of the softening effects of the ladder diagrams on W . Recent works implementing single-shot GW , with approximations different from QSGW, also finds the valence band maximum in CrI_3 at Γ ,^{26,38} which also seems to be confirmed by a recent ARPES study.³⁹

While the band maximum is roughly similar across different levels of theory, there are sharp differences in the overall electronic dispersions and wave functions. Even though the $\widehat{\text{QSGW}}$ band structure more closely resembles DFT than QSGW, the eigenfunctions do not. This can be seen by inspecting the square of the wave function, $|\psi^2|$, corresponding to the highest-lying state at the M point (Fig. 6). The density is plotted in real space, and the abscissa and ordinate are defined by the the inverse transpose of the 2×2 matrix composed of \mathbf{b}_1 and \mathbf{b}_2 of

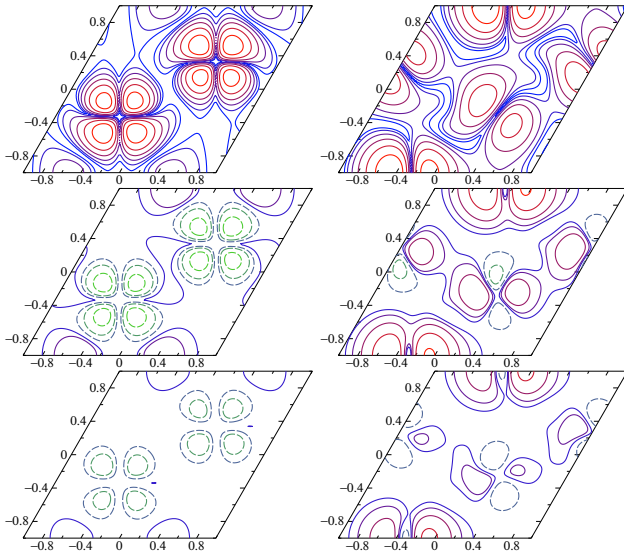


Figure 6. CrBr_3 : Square of wave function ψ , in real space, of the highest valence band state at the M point. All the left panels pass through a Cr plane and right panels pass through a Br plane. Top panels display constant-amplitude contours for DFT eigenfunctions. Contours are taken in half-decade increments in $|\psi|^2$, with a factor of 300 between highest contour (red) and lowest (blue). In the Cr plane, the atomic d_{xy} character centered at Cr nuclei stand in sharp relief; in the Br plane the Br atomic p character is evident. Middle panels show the change in $|\psi|^2$ passing from DFT to QSGW eigenfunctions; bottom panels show the corresponding change passing from DFT to QSGW eigenfunctions. In the bottom four panels, blue→red has a similar meaning as in the top panels (increasing positive $\delta|\psi|^2$), while contours of negative $\delta|\psi|^2$ are depicted by increasing strength in the change blue→green.

Fig. 1. Throughout this paper x and y are defined by aligning \mathbf{b}_2 parallel to y . In this notation the M point is on the \mathbf{b}_2 line, or the y axis. Contour plots in two planes are shown, passing through Cr and Br, respectively. At the LDA level (top panels), the wave function resembles an atomic d_{xy} state centered at each Cr nucleus. In the Br plane some Br p character is evident, and the bond is partially directed along x . The middle panels depict the change in $|\psi|^2$ when passing from DFT to QSGW . Two effects are prominent: first there is a transfer of spectral weight from Cr to Br (mostly green contours on Cr, red on Br) as also noted in Table I. Second, the bonding becomes more directional, forming one-dimensional chains along x . This reflects an enhancement of the Cr-Cr coupling mediated through the Br. It is especially apparent in the Br plane, but it is also reflected in the asymmetry between the x and y directions in the Cr plane. The bottom two panels show the change in $|\psi|^2$ when passing from DFT to QSGW . The effect is similar to $\text{DFT} \rightarrow \text{GW}$, but the magnitude of the change is softened.

The directionality in the wave function is also reflected in strong anisotropy in the valence band mass at the point

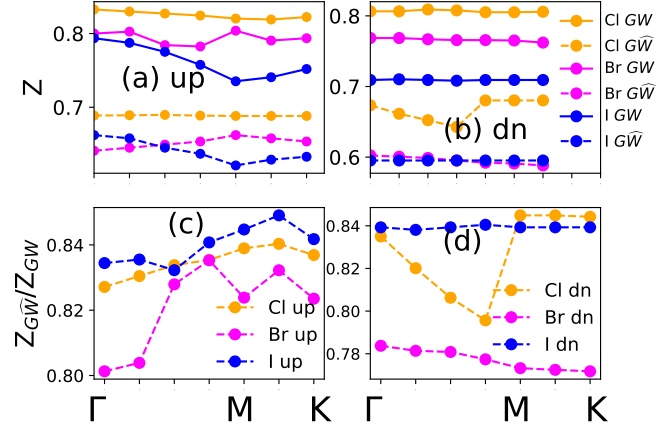


Figure 7. CrX_3 : Real part of $\Sigma(k, \omega)$ is analyzed to extract the quasi-particle renormalization factor Z_k from QSGW and QSGW . (a) and (b) show the weak momentum dependence of the Z_k for the top most valence band at the quasi-particle peaks at the k points chose along the high symmetry directions of the first Brillouin zone for the up and down spin sectors respectively. (c) and (d) show the relative suppression of the Z_k factor in QSGW , compared to QSGW for the up and down spin sectors respectively.

M, particularly in CrBr_3 (see Table. II). By symmetry, there is no anisotropy at the Γ point, but at M it becomes quite pronounced at the highest level of theory.

Finally, we analyze the dynamic and momentum dependent self energies $\Sigma(k, \omega)$ from QSGW and QSGW to further understand the changes in the valence band structure at different levels of theory. We observe that the Σ of the top most valence band has very weak dependence on momentum. The momentum dependence is even weaker in the down spin channel, that is unoccupied. For the up spin channel the momentum dispersion is very similar both in QSGW and QSGW . We extract the quasi-particle renormalization (Z_k) factors from $\Sigma(k, \omega)$ at the quasi-particle energies for the top most valence band. We observe that Z_k reduces by $\sim 20\%$ within QSGW in comparison to QSGW . This suggests that the quasi-particles become further localized at the QSGW level, in comparison to the QSGW . This goes along with charge density that is weakly put back on the atoms at the QSGW level.

Conclusions

We analyze in detail the electronic band structure of CrX_3 within different levels of an *ab initio* theory. The results were interpreted in terms of a simplified tight-binding model to elucidate the trends in $\text{Cl} \rightarrow \text{Br} \rightarrow \text{I}$, in particular the bandgap and the orbital character of the valence band. Many-body effects both enhance the bandgap, and make the valence band eigenfunctions

more directional. We also showed that addition of ladder diagrams to improve W increases the screening, thus softening the many body corrections to DFT. Further we quantify the momentum dependence of the self-energies at different levels of the theory and show explicitly how excitonic correlations lead to re-normalization of the electronic bands and localization of charges. Summarily, we show how a starting point independent implementation of GW and BSE leads to changes in electronic band energies and wavefunctions via complicated interplay between charge and self-energy self-consistencies in CrX_3 .

Acknowledgment

MIK, ANR and SA are supported by the ERC Synergy Grant, project 854843 FASTCORR (Ultrafast dynamics of correlated electrons in solids). MvS and DP are supported by the Simons Many-Electron Collaboration. We acknowledge PRACE for awarding us access to Irene-Rome hosted by TGCC, France and Juwels Booster and Clusters, Germany; STFC Scientific Computing Department's SCARF cluster, Cambridge Tier-2 system operated by the University of Cambridge Research Computing Service (www.hpc.cam.ac.uk) funded by EPSRC Tier-2 capital grant EP/P020259/1.

Appendix A: Numerical Details

Single particle calculations (DFT, and energy band calculations with the static quasiparticlized $QSGW$ self-energy $\Sigma^0(k)$) were performed on a $16 \times 16 \times 1$ k -mesh while the (relatively smooth) dynamical self-energy $\Sigma(k)$ was constructed using a $6 \times 6 \times 1$ k -mesh and $\Sigma^0(k)$ extracted from it. For each iteration in the $QSGW$ self-consistency cycle, the charge density was made self-consistent. The $QSGW$ cycle was iterated until the RMS change in Σ^0 reached 10^{-5} Ry. Thus the calculation was self-consistent in both $\Sigma^0(k)$ and the density. Numerous checks were made to verify that the self-consistent $\Sigma^0(k)$ was independent of starting point, for both $QSGW$ and $QSG\widehat{W}$ calculations; e.g. using LDA or Hartree-Fock self-energy as the initial self energy for $QSGW$ and using LDA or $QSGW$ as the initial self-energy for $QSG\widehat{W}$.

For the present work, the electron-hole two-particle correlations are incorporated within a self-consistent ladder-BSE implementation^{31,32} with Tamm-Dancoff approximation.^{40,41} The effective interaction W is calculated with ladder-BSE corrections and the self energy, using a static vertex in the BSE. G and W are updated iteratively until all of them converge and this is what we call $QSG\widehat{W}$. Ladders increase the screening of W , reducing the gap besides softening the LDA \rightarrow $QSGW$ corrections noted for the valence bands.

For all materials, we checked the convergence in the $QSG\widehat{W}$ band gap by increasing the size of the two-particle Hamiltonian. We increase the number of va-

variants	CrCl ₃	CrBr ₃	CrI ₃
DFT	4.23	4.44	4.66
QSGW	4.08	4.3	4.66
BSE	4.11	4.35	4.64

Table III. Shown are the Cr-d occupancies.

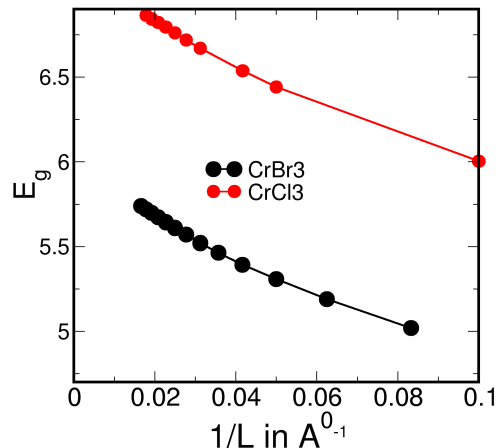


Figure 8. CrBr₃ and CrCl₃ : Scaling of the one particle band gap from $QSGW$ with vacuum size L .

lence and conduction states that are included in the two-particle Hamiltonian. We observe that for all materials the $QSG\widehat{W}$ band gap stops changing once 24 valence and 24 conduction states are included in the two-particle Hamiltonian. While the gap is most sensitive to the number of valence states, 14 conducting states produces results within 2% error of the converged results from 24 conduction states.

In Tab. III we list the Cr-d occupancies for different materials at different levels of the theory.

Appendix B: Vacuum Distance Scaling

Periodic boundary conditions were used in all directions, introducing an unwanted coupling between CrBr₃ slabs. To minimize this coupling a vacuum of length L was inserted between slabs, and L was varied.

As is well known, the $QSGW$ is known to fix the infamous ‘gap problem’⁷⁴² in insulators, we observe that the band gap increases significantly in all three compounds within $QSGW$; 6.87 eV in Cl, 5.73 eV in Br and 3.25 eV in I (see I). We change the vacuum length from 10 Å to 80 Å, and observe the scaling of the band gap with vacuum size (L). We observe an almost perfect $1/L$ scaling (see Fig. 8) of the gap as noted earlier in a separate work on V_2O_5 .⁴³ This also allows us to check the dielectric constant (ϵ_∞) and its vacuum correction. In the limit of a purely free standing monolayer all three direc-

tional components of the macroscopic dielectric response in the static limit approaches 1, suggesting the absence of screening. We use this vacuum length (60 Å) for the rest of the discussions in the present work.

Appendix C: Full Band Structures

In Fig. 9 we show the band structures for all materials over larger energy windows.

-
- * swagata.acharya@ru.nl
- ¹ B. Huang, G. Clark, E. Navarro-Moratalla, D. R. Klein, R. Cheng, K. L. Seyler, D. Zhong, E. Schmidgall, M. A. McGuire, D. H. Cobden, *et al.*, *Nature* **546**, 270 (2017).
 - ² D. R. Klein, D. MacNeill, J. L. Lado, D. Soriano, E. Navarro-Moratalla, K. Watanabe, T. Taniguchi, S. Manni, P. Canfield, J. Fernández-Rossier, *et al.*, *Science* **360**, 1218 (2018).
 - ³ Z. Zhang, J. Shang, C. Jiang, A. Rasmita, W. Gao, and T. Yu, *Nano letters* **19**, 3138 (2019).
 - ⁴ M. Kim, P. Kumaravadeivel, J. Birkbeck, W. Kuang, S. G. Xu, D. Hopkinson, J. Knolle, P. A. McClarty, A. Berdyugin, M. B. Shalom, *et al.*, *Nature Electronics* **2**, 457 (2019).
 - ⁵ X. Cai, T. Song, N. P. Wilson, G. Clark, M. He, X. Zhang, T. Taniguchi, K. Watanabe, W. Yao, D. Xiao, *et al.*, *Nano letters* **19**, 3993 (2019).
 - ⁶ C. Gong, L. Li, Z. Li, H. Ji, A. Stern, Y. Xia, T. Cao, W. Bao, C. Wang, Y. Wang, *et al.*, *Nature* **546**, 265 (2017).
 - ⁷ Z. Fei, B. Huang, P. Malinowski, W. Wang, T. Song, J. Sanchez, W. Yao, D. Xiao, X. Zhu, A. F. May, *et al.*, *Nature materials* **17**, 778 (2018).
 - ⁸ Y. Deng, Y. Yu, M. Z. Shi, Z. Guo, Z. Xu, J. Wang, X. H. Chen, and Y. Zhang, *Science* **367**, 895 (2020).
 - ⁹ C. Gong and X. Zhang, *Science* **363** (2019).
 - ¹⁰ M. Gibertini, M. Koperski, A. Morpurgo, and K. Novoselov, *Nature nanotechnology* **14**, 408 (2019).
 - ¹¹ N. D. Mermin and H. Wagner, *Physical Review Letters* **17**, 1133 (1966).
 - ¹² V. Y. Irkhin, A. Katanin, and M. Katsnelson, *Physical Review B* **60**, 1082 (1999).
 - ¹³ D. Soriano, M. I. Katsnelson, and J. Fernández-Rossier, *Nano Letters* **20**, 6225 (2020).
 - ¹⁴ S. Jiang, L. Li, Z. Wang, K. F. Mak, and J. Shan, *Nature nanotechnology* **13**, 549 (2018).
 - ¹⁵ S. Jiang, J. Shan, and K. F. Mak, *Nature materials* **17**, 406 (2018).
 - ¹⁶ Z. Wang, T. Zhang, M. Ding, B. Dong, Y. Li, M. Chen, X. Li, J. Huang, H. Wang, X. Zhao, *et al.*, *Nature nanotechnology* **13**, 554 (2018).
 - ¹⁷ M. Bonilla, S. Kolekar, Y. Ma, H. C. Diaz, V. Kalappattil, R. Das, T. Eggers, H. R. Gutierrez, M.-H. Phan, and M. Batzill, *Nature nanotechnology* **13**, 289 (2018).
 - ¹⁸ S. Jiang, L. Li, Z. Wang, J. Shan, and K. F. Mak, *arXiv preprint arXiv:1807.04898* (2018).
 - ¹⁹ T. Song, X. Cai, M. W.-Y. Tu, X. Zhang, B. Huang, N. P. Wilson, K. L. Seyler, L. Zhu, T. Taniguchi, K. Watanabe, *et al.*, *Science* **360**, 1214 (2018).
 - ²⁰ T. Song, M. W.-Y. Tu, C. Carnahan, X. Cai, T. Taniguchi, K. Watanabe, M. A. McGuire, D. H. Cobden, D. Xiao, W. Yao, *et al.*, *Nano letters* **19**, 915 (2019).
 - ²¹ Z. Wang, I. Gutiérrez-Lezama, N. Ubrig, M. Kroner, M. Gibertini, T. Taniguchi, K. Watanabe, A. Imamoğlu, E. Giannini, and A. F. Morpurgo, *Nature communications* **9**, 1 (2018).
 - ²² H. H. Kim, B. Yang, T. Patel, F. Sfigakis, C. Li, S. Tian, H. Lei, and A. W. Tsen, *Nano letters* **18**, 4885 (2018).
 - ²³ I. Kashin, V. Mazurenko, M. Katsnelson, and A. Rudenko, *2D Materials* **7**, 025036 (2020).
 - ²⁴ Y. Kvashnin, A. Bergman, A. Lichtenstein, and M. Katsnelson, *Physical Review B* **102**, 115162 (2020).
 - ²⁵ D. Soriano, A. N. Rudenko, M. I. Katsnelson, and M. Röser, “Environmental screening and ligand-field effects to magnetism in CrI_3 monolayer,” (2021), *arXiv:2103.04686 [cond-mat.str-el]*.
 - ²⁶ A. Molina-Sanchez, G. Catarina, D. Sangalli, and J. Fernandez-Rossier, *Journal of Materials Chemistry C* **8**, 8856 (2020).
 - ²⁷ S. V. Streltsov and D. I. Khomskii, *Physics-Uspekhi* **60**, 1121 (2017).
 - ²⁸ D. Soriano, C. Cardoso, and J. Fernández-Rossier, *Solid State Communications* **299**, 113662 (2019).
 - ²⁹ M. van Schilfgaarde, T. Kotani, and S. Faleev, *Physical review letters* **96**, 226402 (2006).
 - ³⁰ D. Pashov, S. Acharya, W. R. Lambrecht, J. Jackson, K. D. Belashchenko, A. Chantis, F. Jamet, and M. van Schilfgaarde, *Computer Physics Communications* **249**, 107065 (2020).
 - ³¹ B. Cunningham, M. Grüning, P. Azarhoosh, D. Pashov, and M. van Schilfgaarde, *Physical Review Materials* **2**, 034603 (2018).
 - ³² B. Cunningham, M. Gruening, D. Pashov, and M. van Schilfgaarde, “Qsgw: Quasiparticle self consistent gw with ladder diagrams in w,” (2021), *arXiv:2106.05759 [cond-mat.mtrl-sci]*.
 - ³³ S. Albrecht, L. Reining, R. Del Sole, and G. Onida, *Physical review letters* **80**, 4510 (1998).
 - ³⁴ M. Rohlfing and S. G. Louie, *Physical Review B* **62**, 4927 (2000).
 - ³⁵ A. N. Chantis, M. van Schilfgaarde, and T. Kotani, *Physical review letters* **96**, 086405 (2006).
 - ³⁶ C. Bhandari, M. van Schilfgaarde, T. Kotani, and W. R. Lambrecht, *Physical Review Materials* **2**, 013807 (2018).
 - ³⁷ D. Deguchi, K. Sato, H. Kino, and T. Kotani, *Japanese Journal of Applied Physics* **55**, 051201 (2016).
 - ³⁸ M. Wu, Z. Li, T. Cao, and S. G. Louie, *Nature communications* **10**, 1 (2019).
 - ³⁹ A. K. Kundu, Y. Liu, C. Petrovic, and T. Valla, *Scientific reports* **10**, 1 (2020).
 - ⁴⁰ S. Hirata and M. Head-Gordon, *Chemical Physics Letters* **314**, 291 (1999).
 - ⁴¹ G. Myrta, A. Marini, and X. Gonze, *Nano Letters* **9**, 2820 (2009).
 - ⁴² F. Aryasetiawan and O. Gunnarsson, *Reports on Progress in Physics* **61**, 237 (1998).
 - ⁴³ C. Bhandari, W. R. Lambrecht, and M. van Schilfgaarde, *Physical Review B* **91**, 125116 (2015).

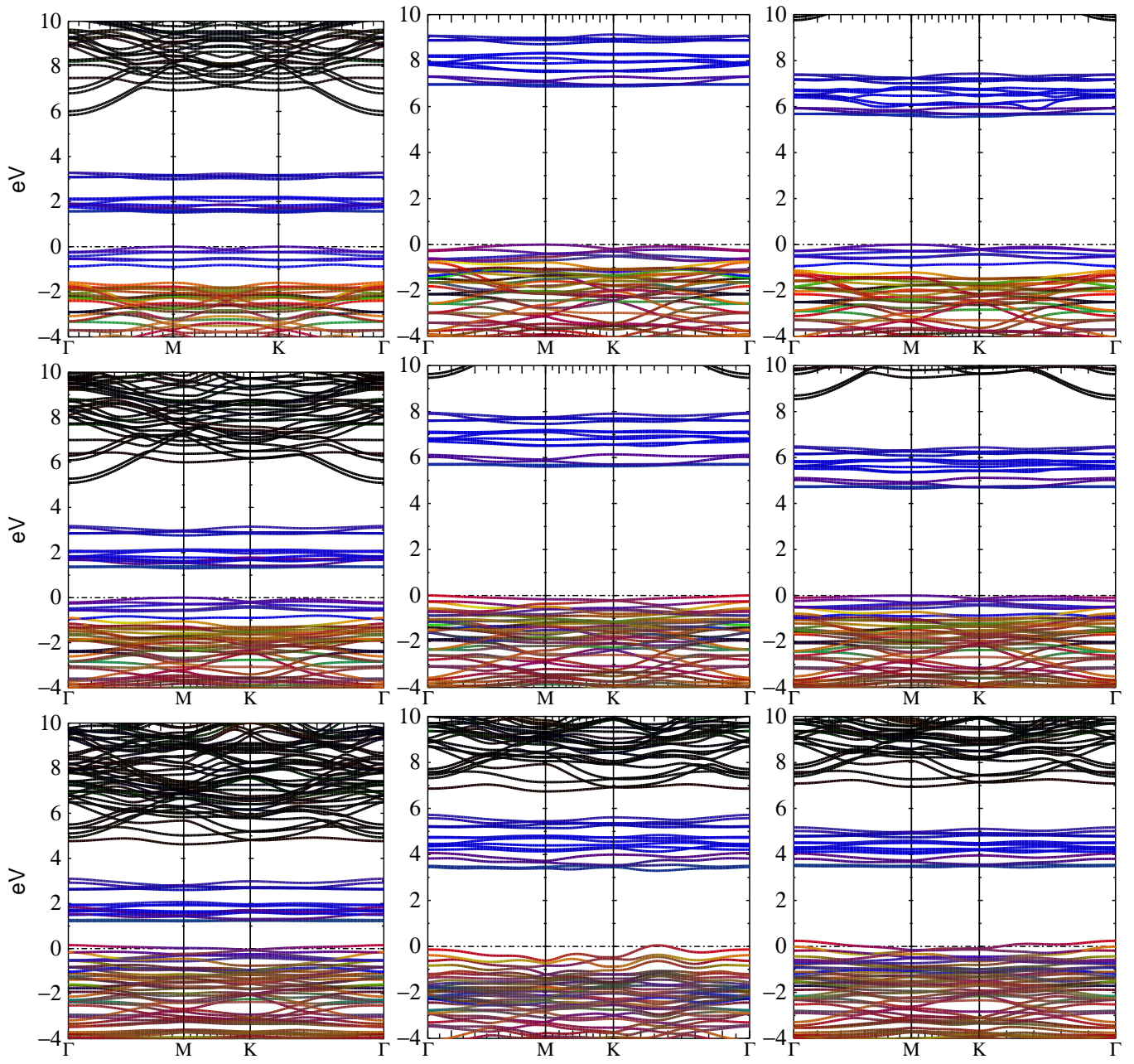


Figure 9. CrX_3 : Top panels is for $X = \text{Cl}$, middle one for Br and bottom one for I . The colors correspond to $X-p_x + p_y$ (red), $X p_z$ (green), Cr-d (blue) (From left to right: DFT, QSGW and QSGW respectively).